RSC Advances

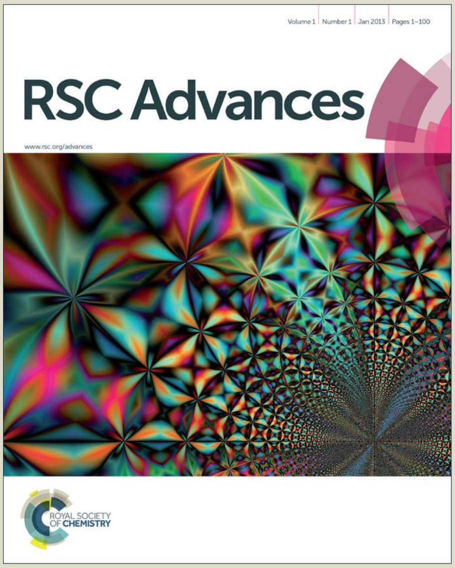

ROYAL SOCIETY OF CHEMISTRY

www.rsc.org/advances

Synthesis and electrochemical properties of monoclinic fluorine-doped lithium manganese oxide ($Li_xMnO_{2-y}F_y$) for lithium secondary batteries

Yu Zhang Zhi Su* Xiang Yao Yingbo Wang

(College of Chemistry and Chemical Engineering , Xinjiang Normal University, Urumqi, 830054, Xinjiang, China)

Corresponding author. Tel.: +86- 991-4332683; fax: +86-991-4332683.

E-mail address: suzhixj@sina.com (Z. Su).

Abstract

A series of monoclinic fluorine-doped lithium manganese oxide ($Li_xMnO_{2-y}F_y$) were prepared by the ion exchange of sodium for lithium in $Na_xMnO_{2-y}F_y$ precursors that were obtained using a high-temperature solid-state reaction. The microstructure and composition of the samples were characterized by X-ray diffraction (XRD), scanning electron microscopy (SEM), inductively coupled plasma atomic emission spectroscopy (ICP-AES), ion chromatography(IC), fourier transform infrared spectroscopy (FTIR), and X-ray photoelectron spectroscopy (XPS). The different valence states of manganese in material $Li_xMnO_{2-y}F_y$ were determined by redox titration method. The electrochemical performance of these samples as cathode materials were studied by the galvanostatic and cyclic voltammetry method. These materials had a high crystallite size, which was composed of 5–8μm grains. The $Li_{0.86}MnO_{1.98}F_{0.02}$ materials delivered an initial discharge capacity of 129.2 mAh/g and gradually increased to a maximum discharge capacity of 210 mAh/g at a current density of 50 mA/g after 50 cycles. Moreover, the material showed an excellent cycling behavior, even though its original structure transformed into the spinel phase during cycling. The results show that the partial substitution of monoclinic $LiMnO_2$ with fluorine can improve the cycle stability and high-rate discharge capability of cathode materials.

Keywords: Monoclinic $LiMnO_2$; Fluorine substitution; High-temperature solid state synthesis; Cathode materials;Redox titration

1. Introduction

Lithium manganese oxide ($LiMnO_2$) compounds have received attention as intercalation cathodes for rechargeable Li batteries due to their high theoretical capacity, low cost, and nontoxicity, and there has been significant interest in monoclinic $LiMnO_2$ (space group *C2/m*, hereafter denoted as *m*-$LiMnO_2$) as a potential cathode material for replacing $LiCoO_2$, which is the currently used cathode material in commercial Li-ion rechargeable batteries [1–3]. However, *m*-$LiMnO_2$ is generally considered to be unstable compared to orthorhombic $LiMnO_2$ (space group Pmnm, hereafter denoted as *o*-$LiMnO_2$) [4]. One significant drawback is the difficult synthesis of layered *m*-$LiMnO_2$ using the conventional high-temperature solid-state reaction method because these methods always produce *o*-$LiMnO_2$ [5–6]. Consequently, m-$LiMnO_2$ was first obtained by metastable synthesis routes such as ion exchange and hydrothermal reactions [7–8].

In this compound, the O^{2-} ions are arranged in a cubic close-packed structure, and the octahedral interstices are occupied by Li^+ and Mn^{3+} with layered cation ordering. The neighboring MnO_6 octahedra share a common edge. Due to the presence of high-spin Mn^{3+} on the octahedral sites, the local site symmetry around Mn^{3+} is distorted from a regular octahedron, and the overall crystal structure is monoclinic due to the cooperative Jahn-Teller distortion. Therefore, it is difficult to inhibit the irreversible structural transformation from layered $LiMnO_2$ to a spinel $LiMnO_2$ during electrochemical cycling. According to the first-principles calculations, the Jahn-Teller effect should be absent in the low-spin state, and the layered structure could be stabilized in *m*-$LiMnO_2$ [9].

Cation doping protects the layered monoclinic structure against Jahn-Teller distortion [10] and has superior Li insertion/extraction cycling properties for *m*-$LiMnO_2$. Many studies have focused on stabilization of the layered material structure, particularly for *m*-$LiMnO_2$, by partial substitution of Mn by Cr, Al, Co, Ni and Mg [11–18]. However, for *m*-$LiMnO_2$ to be suitable for practical applications such as high-energy and power density applications, further stabilization of the monoclinic structure is needed. Small amounts of additional dopants such as fluorine [19] into the $Li(Ni_{1/3}Co_{1/3}Mn_{1/3})O_2$ lattice have been reported to improve the structural stability and enhance the cycling performance. Zheng et al. prepared the $Li[Li_{0.2}Mn_{0.54}Ni_{0.13}Co_{0.13]}O_{2-x}F_x$ (x=0, 0.05 and 0.10) composite materials with different content of fluorine by sol–gel method using NH_4F as fluorine source. XRD and XPS analysis shows that the fluorine ions successfully substitute for oxygen sites. The F-doped $Li[Li_{0.2}Mn_{0.54}Ni_{0.13}Co_{0.13]}O_{2-x}F_x$ materials show superior cycling performance [20]. In fact, Jouanneau et al. discussed the influence of LiF additions on $Li(Ni_xCo_{1-2x}Mn_x)O_2$ and found that materials could be obtained using LiF as a sintering agent with almost no disturbance of the cell performance [21–23].

In this work, we attempt to prepare a partial substitution of O^{2-} anions by F^- anions layered monoclinic $LiMnO_2$ using a high-temperature solid-state reaction method with a subsequent ion-exchange reaction. The morphology, microstructure, composition, and electrochemical properties were investigated in detail to assess the suitability of these samples as cathode materials.

2. Experimental

2.1 Preparation and characterization

First, $Mn(CH_3COO)_2.4H_2O$ was heated with the ramping rate of 2°C/min and decomposed at 500ºC for 15 h in air to produce Mn_2O_3. Samples of monoclinic α-$NaMnO_2$ were prepared using a solid-state reaction of the stoichiometric mixture of Mn_2O_3 (0.01 mol, 1.58 g) and Na_2CO_3 (Na/Mn=1.1, 0.011 mol, 1.16 g) in a closed crucible at 750ºC for 24 h in air. The mixture was quenched to room temperature and ground, and the process was repeated. The resulting samples were stored in a desiccator. In the subsequent ion-exchange reaction, 1 g of *α*-$NaMnO_2$ was mixed with 10 g LiCl in 40 ml n-hexanol and autoclaved at 150°C for 12 h in a 50 ml teflon-lined stainless steel vessel. The obtained m-$LiMnO_2$ products were washed with de-ionized water and then dried in an oven at 105°C for 12 h. Fluorine-substituted materials were prepared with the molar ratio of F/Mn of 0.01/1, 0.03/1, and 0.05/1 with the homogeneous mixture of NH_4F of 0.001 mol, 0.037 g; 0.003 mol, 0.0111 g; and 0.005 mol, 0.0185 g, respectively The final fluorine-substituted materials were obtained by the above-mentioned method.

The microstructure of the as-prepared samples was characterized by X-ray diffraction (XRD, Rigaku D/max-2500) with CuKα radiation and scanning electron microscopy (SEM, HITACHI S-3500N). Elemental analysis for Na, Li, and Mn were performed using inductively coupled plasma atomic emission spectroscopy (ICP-AES, IRIS Advantage) and the content of fluorine by ion chromatography (ICS-2100) to determine the chemical composition of these materials. The Fourier transform infrared spectra (FTIR) of these samples were recorded from 400 to 4000 cm^{-1} at room temperature using the KBr wafer technique in a Bio-Rad FTS 6000 FTIR instrument with a resolution of 2 cm^{-1} in transmittance mode. The surface chemical state was recorded using X-ray photoelectron spectroscopy (XPS, PHI-5300 ESCA)

2.2 Determination of material composition

The sample was treated by HCl , HNO_3 and HF at room temperature, H_3BO_3 was added to complex with excessive fluoride ions. Working conditions of the instrument was optimized, appropriate analysis line of various elements was selected and the internal standard method was used to eliminate disturbance with yttrium selected as internal standard element, the content of lithium and manganese were determinied by inductively coupled plasma emission spectroscopy (ICP-AES).The sample was decomposed by H_2SO_4. After water steam distillation at 160-180□, the fluoride in testing solution would be relersed and absorbed by NaOH solution realizing the separation from matrix and other elements. Then, the content of fluoride was determinied by ion chromatography(IC).

2.3 Analysis of the valence states of manganese

The total amount of manganese was determined by chemical conversion to permanganic radical using acidified ammonium persulfate, the determination of Mn^{4+} by the acetylacetone-iodometric method being carried out in the presence of Mn^{3+} without its interference , and the amount of the tetravalent and trivalent manganese being determined by dissolving the lithium manganese oxides in a known excess of ammonium iron sulfate in 1 mol·L^{-1} sulfuric acid and back-titrating the unreacted Fe^{2+} with standardized potassium dichromate .Based on the results obtained , the amount of bivalent manganese and average manganic valence could be calculated[24].

2.4 Electrochemical performance

The working electrode was prepared by compressing a mixture of the active materials with acetylene black and a binder (polytetrafluoroethylene, PTFE) in a weight ratio of 75:20:5. Lithium metal was used for the counter and reference electrodes. The electrolyte was $LiPF_6$ (1 M) in a mixture of ethylene carbonate (EC), dimethyl carbonate (DMC), and ethyl methyl carbonate (EMC) in a weight ratio of 1:1:1. All procedures for handing and fabricating the electrochemical cells were performed in an argon-filled glove box. The galvanostatic method was used to measure the electrochemical capacity and cycle life of the electrodes under the charge-discharge current density of 50 mA/g at room temperature using a LAND CT2001A instrument. The cut-off potentials for the charge and discharge were set between 2.0–4.3 V (vs. Li^+/Li). Cyclic voltammetry (CV) was performed with a LK2500 electrochemical workstation, scanning from 2 to 4.3 V with a scan rate of 0.1 mV/s. The electrochemical impedance spectra (EIS) were measured using a Zahner IM6ex electrochemical workstation over the frequency ranges from 10 kHz to 10 mHz with a 5-mV AC input signal applied between the working and reference electrodes.

3. Results and discussion

3.1 Composition and structure

The composition of the as-prepared samples, which were calculated from the results of ICP-AES , and IC determination and valence state of Mn analysis, are summarized in Table 1. For all samples, most of the Na^+ cation can be exchanged and lithium concentration can be controlled at about 0.90 in unit. All of the XRD patterns were refined by the Rietveld analysis, an example of the Rietveld refinement is shown in Fig. 1 for the composition of $Li_xMnO_{2-y}F_y$. All diffraction peaks, except for the market peaks, could be attributed to the small amount of monoclinic $Na_{0.7}MnO_{2.05}$ because $NaMnO_2$ was not stable and was very hygroscopic in air; $NaMnO_2$ was easily transformed to the more stable phase of $Na_{0.7}MnO_{2.05}$[25].

Table 1 Chemical composition of the *m*-$LiMnO_2$ and F-substituted *m*-$LiMnO_2$.

Sample	Design formula	Precursor powders	Valenceof manganese	Chemical composition
a	$NaMnO_2$	$Na_{0.96}MnO_2$	3.04	$Na_{0.96}MnO_2$
b	$LiMnO_2$	$Na_{0.91}MnO_2$	3.09	$Na_{0.06}Li_{0.85}MnO_2$
c	$LiMnO_{1.99}F_{0.01}$	$Na_{0.90}MnO_{1.98}F_{0.02}$	3.08	$Na_{0.05}Li_{0.86}MnO_{1.98}F_{0.02}$
d	$LiMnO_{1.97}F_{0.03}$	$Na_{0.91}MnO_{1.96}F_{0.04}$	3.05	$Na_{0.06}Li_{0.88}MnO_{1.96}F_{0.04}$
e	$LiMnO_{1.95}F_{0.05}$	$Na_{0.92}MnO_{1.93}F_{0.07}$	3.01	$Na_{0.06}Li_{0.87}MnO_{1.93}F_{0.07}$

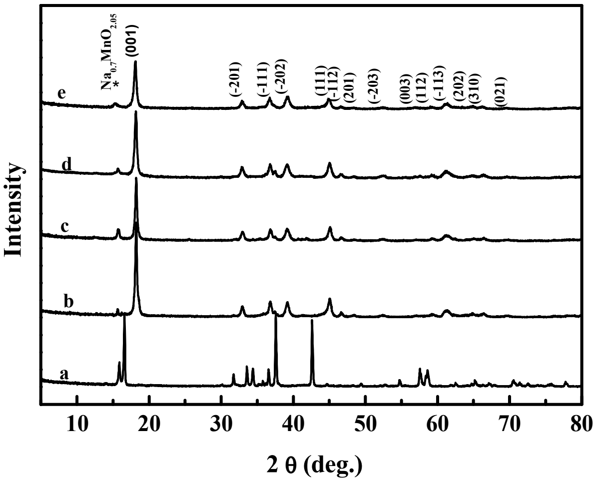

Fig. 1 The XRD patterns of the as-prepared samples: (a) $Na_{0.96}MnO_2$, (b) $Na_{0.06}Li_{0.85}MnO_2$, (c) $Na_{0.05}Li_{0.86}MnO_{1.98}F_{0.02}$, (d) $Na_{0.06}Li_{0.88}MnO_{1.96}F_{0.04}$, and (e) $Na_{0.06}Li_{0.87}MnO_{1.93}F_{0.07}$.

The Table 2 list the comparison between the observed values and the JCPDS-87155 standard card data. The characteristics of the synthetic product crystal plane diffraction spacing and diffraction angle all can correspond well, the as-prepared samples could be assigned to the monoclinic structure with space group of C_2/m, which differs from o-$LiMnO_2$[7–9]. At the same time the characteristic peak of α-$NaMnO_2$ are not appear noticeably in XRD, this shows that ion exchange basic completely. Moreover, We also find that the observed dhkl values is greater than the standard and the 2θ values is opposite. This may be due to the material contains no exchange of sodium(sodium ions with greater radius than lithium ion).

Table 2 Comparison between the observed and JCPDS-871255 values

	$d_{hkl}(LiMnO_2)$/nm		2θ/(º)	
h k l	Observed	JCPDS	Observed	JCPDS
0 0 1	0.4849	0.4842	18.28	18.31
-2 0 1	0.2712	0.2711	33.02	33.01
1 1 0	0.2440	0.2435	36.80	36.89
-1 1 1	0.2397	0.2395	37.48	37.50
-2 0 2	0.2298	0.2295	39.12	39.21
1 1 1	0.2012	0.2006	45.02	45.15
-1 1 2	0.1942	0.1942	46.46	46.74
2 0 1	0.1878	0.1875	48.45	48.49
0 0 3	0.1626	0.1614	56.52	57.01
1 1 2	0.1560	0.1555	59.16	59.37
-1 1 3	0.1511	0.1505	61.26	61.56
-3 1 2	0.1493	0.1487	62.12	62.36
0 2 0	0.1407	0.1404	66.34	66.53
0 2 1	0.1350	0.1348	69.54	69.66

Lattice parameters of all samples obtained from the rietveld refinement are listed in Table 3. With increasing fluorine content, cell volume increased from 0.0824 nm^3 to 0.0839 nm^3, the increase of cell volume is attributed to the replacement of O^{2-} (r = 0.132nm) with greater F^- (r = 0.136nm) , which are in agreement with literature values [26]. From the table can be found that the increase of the content of fluorine can decrease the valence state of Mn in material. The results attributable to the low valence state of anion (F^-) supersedes the high valence state O^{2-}, and it also demonstrated that the fluorine ions successfully doped into the lattice structure.

Table 3 Lattice parameters of the samples after Rietveld refinement

Sample	a(nm)	b(nm)	c(nm)	cell volume(nm^3)
$Na_{0.96}MnO_2$	0.582	0.287	0.576	0.0962
$Na_{0.06}Li_{0.85}MnO_2$	0.544	0.281	0.539	0.0824
$Na_{0.05}Li_{0.86}MnO_{1.98}F_{0.02}$	0.543	0.282	0.541	0.0828
$Na_{0.06}Li_{0.88}MnO_{1.96}F_{0.04}$	0.543	0.282	0.543	0.0831
$Na_{0.06}Li_{0.87}MnO_{1.93}F_{0.07}$	0.544	0.283	0.549	0.0839

The FTIR spectra of these as-prepared samples are indicated in Fig. 2. The bands in the region of 3000–3500 cm^{-1} can be assigned to OH stretching vibrations. Moreover, the bending mode vibration of water is observed at 1600–1800 cm^{-1}. The weak absorptions at 2832 and 2886 cm^{-1} are due to C-H stretching models, and the bands at around 1475 and 2465 cm^{-1} result from the absorption of the C=O group [27]. Two obvious absorption bands are observed in the infrared (IR) spectra of these materials at around 875 and 993 cm^{-1} (except for $Na_{0.96}MnO_2$ samples), which could be attributed to the metal hydroxide vibration band [28]. Furthermore, the IR bands in the region of 450-750 cm^{-1} could be assigned to Mn-O stretching vibrations in lithium-manganese-oxide compounds [29].

For the $Na_{0.96}MnO_2$ and $Na_{0.06}Li_{0.85}MnO_2$ samples, one featured band at 530cm^{-1} is observed. However, for the F-doped sample of $Na_{0.05}Li_{0.86}MnO_{1.98}F_{0.02}$, an obvious blue shift is observed in the Mn-O stretching band from 532 to 550 cm^{-1}. The electronegativity of F (4.0), which is higher than that of O (3.5), can strengthen the Mn-O stretching bands, whereas the thermochemical radius of F^- (0.136 nm) is greater than the O^{2-} ionic radius (0.132 nm), leading to the blue shift[30]. Certainly, with the fluoride concentration increase, the blue shift will become more obviously which causes the oxygen defects concentration increase in the material. Due to the deficiency of oxygen ion in the electrode material caused by oxygen defects, there are positive charged oxygen vacancies in the structure; and then during the immersion of electrolytic solution to electrode surface, more oxygen defects produce thicker organic electrolytic liquid film, which arise the organic electrolytic liquid film resistance. This result implies that oxygen defects will reduce the electrochemical capacity and cycling performance of the electrode material; and this is in agreement with the electrochemical performance test results shown below [31].

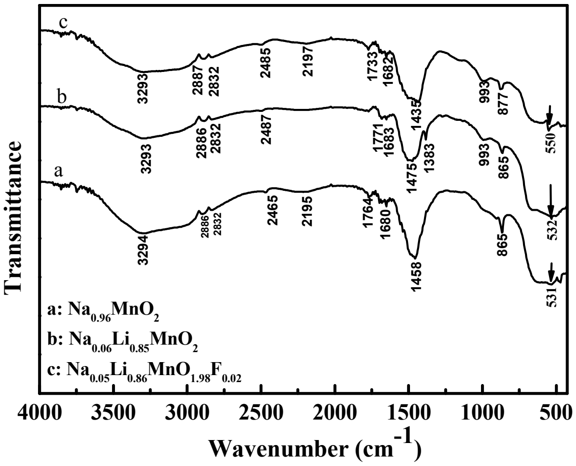

Fig. 2 The IR spectra of (a) $Na_{0.97}MnO_2$, (b) $Na_{0.07}Li_{0.85}MnO_2$, and (c) $Na_{0.06}Li_{0.86}MnO_{1.98}F_{0.02}$.

Fig. 3 shows the SEM images of the as-prepared samples. The layered $Na_{0.97}MnO_2$ and monoclinic $Li_xMnO_{2-y}F_y$ samples have a similar bar-shaped morphology with a grain diameter of 5–8μm and with small particles of about 2–3 μm in size. However, A topotactic reaction can be observed in a morphology changes from the SEM . Small particles can be found in Fig. 3. The things is especially obvious with the increase of fluorine content .The results should be attributed to the primary particles become well-developed when the amount of fluorine increases. Changes of morphology reveal that incorporation of fluorine alters the surface energy and catalyzes the growth of the primary particles, consistent with that reported for other cathode materials with fluorine doping [32,33].

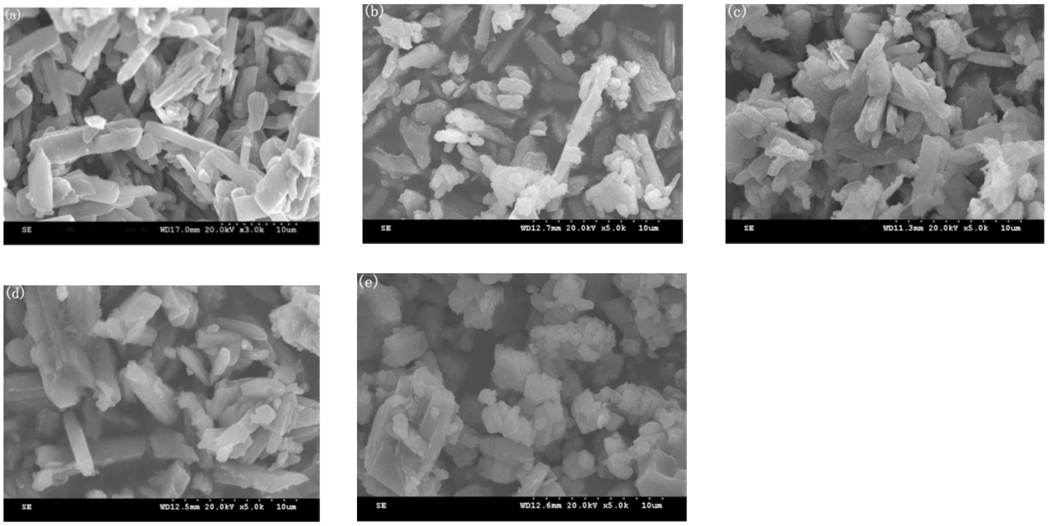

Fig. 3 The SEM images of the as-prepared samples: (a) $Na_{0.96}MnO_2$, (b) $Na_{0.06}Li_{0.85}MnO_2$, (c) $Na_{0.05}Li_{0.86}MnO_{1.98}F_{0.02}$, (d) $Na_{0.06}Li_{0.88}MnO_{1.96}F_{0.04}$, and (e) $Na_{0.06}Li_{0.87}MnO_{1.93}F_{0.07}$.

3.2 Electrochemical properties

Fig. 4 exhibits the initial charge/discharge curves of $Li_xMnO_{2-y}F_y$ (y=0, 0.02, 0.04, 0.07) at a current density of 50 mA g^{-1} (0.2 C) between 2.0 and 4.3 V. An initial discharge capacity of 133.2 mAh/g is obtained for the $Na_{0.06}Li_{0.85}MnO_2$ sample, which is obviously higher than that of *o*-$LiMnO_2$ obtained using the conventional high-temperature solid reaction. With the increase of fluorine content, the discharge capacities of the initial discharge capacity is decreased to 129.2 mAh/g at 0.2C for $Na_{0.05}Li_{0.86}MnO_{1.98}F_{0.02}$, the initial discharge capacities of $Na_{0.06}Li_{0.88}MnO_{1.96}F_{0.04}$ and $Na_{0.06}Li_{0.87}MnO_{1.93}F_{0.07}$ are 120.6 and 112.3 mAh/g, respectively. This is because the fluorine is a inactive substances and atomic weight of fluorine (19 g/mol)) slightly larger than oxygen atomic weight(16g/mol). Moreover, fluorine substituted materials exhibit higher charging voltage over the potential range and the discharge plateau is lower than the pristine one, which is an indication of the higher polarization effect. This similar phenomena, which is ascribed to the stronger bonding strength of Li-F (577 kJ mol^{-1}) bond than the Li-O bond (341 kJ mol^{-1}), are also observed and explained by previous researchers [34,35].

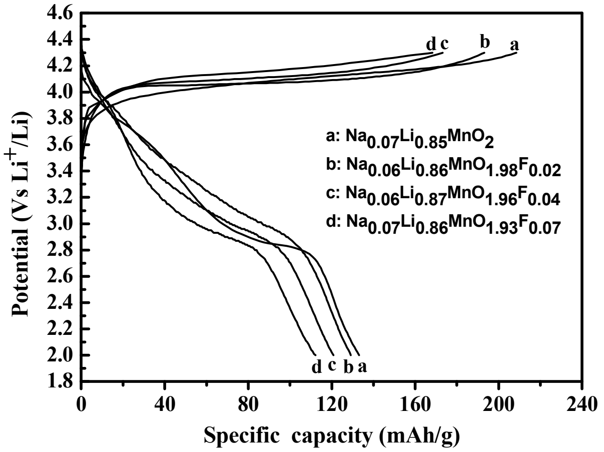

Fig. 4 The initial charge–discharge voltage profile (a), differential capacity plots(b) of $Li_xMnO_{2-y}F_y$ (y=0,0.02,0.04,0.07) when cycled between 2.0 and 4.3 V at a current density of 50 mA/g

The rate capabilities of the materials are operated at the same current densities between 2.0 and 4.3 V. Fig. 5 compares the discharge capacities of the electrodes at various C rates.The results of the electrochemical cycles indicated that the discharge capacity of monoclinic $LiMnO_2$ was small at the initial cycles, gradually increased with increasing cycle number, and the capacity finally stabilized. This result was consistent with the previously reported results of orthorhombic $LiMnO_2$ electrochemical cycle behavior. This phenomenon reveals that monoclinic $LiMnO_2$ cathode materials undergo an activation process during the electrochemical cycle, during which there is a phase transition from *m*-$LiMnO_2$ to cubic spinel $Li_xMn_2O_4$ [36].In comparison, the cycle stability of the $Na_{0.06}Li_{0.85}MnO_2$ sample is poor with a low capacity retention of 80.8 mAh/g after 50 cycles. However, the fluorine substituted materials show better rate capability at high Charge and dischanrg rates. The capacity retention of these materials is significantly improved by fluorine substitution, The good rate capability of fluorine substituted materials could be attributed to the existence of the strong bonding by fluorine which stabilizes the host structure and increases the stability of cathode materials [37]. The results also show that the electrochemical performances of the materials were severely damaged with the fluorine content increased, This is related to the amount of oxygen defects in materials. Therefore, the fluorine content should be controlled in order to prevent more oxygen defects in synthetic materials . In other words, the partial fluorine substitution in the layered monoclinic structure can significantly depress this structural transformation and slow the rate of capacity decay.

We also notice that the Na^+ cation can be reserved at about 0.06 in unit in all samples. The Na^+ ionic radius (0.097 nm) is larger than the Li^+ ionic radius (0.060 nm). Thus, in monoclinic Na-substituted Li_xMnO_2, the small change of the interlayer spacing to accommodate Na allows high rechargeability and good cycle life. This result could be explained by the extraction of a limited amount of sodium ions from the interlayer spacing while maintaining the layered structure upon cycling [38].

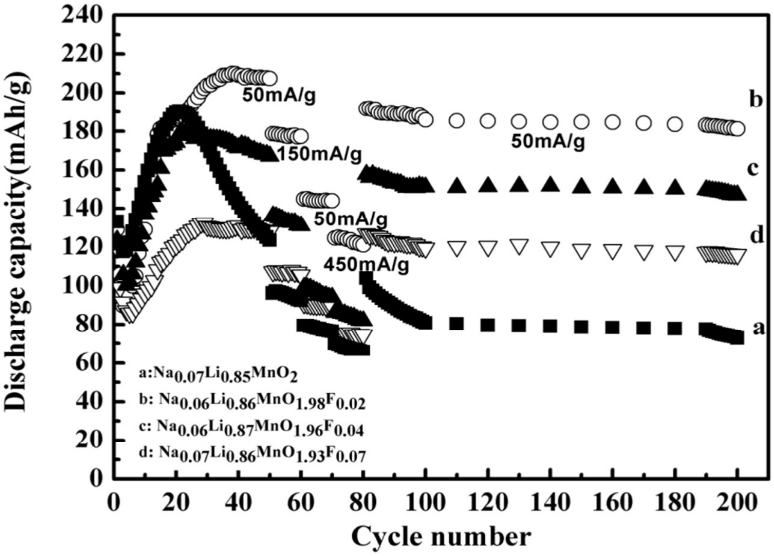

Fig. 5 Cycle performance of the as-prepared samples at different discharge current densities (charging at 50 mA/g).

Initial investigation of $Li_xMnO_{2-y}F_y$ were carried out using cyclic voltammetry, Fig. 6. A rate of 0.01 mV/ s between potential limits of 2 and 4.3 V was employed. Cycling commenced with oxidation from the open circuit potential of 2 V. Fig.6(a) and Fig.6(b) shows typical cyclic voltammograms of the $Na_{0.06}Li_{0.85}MnO_2$ and $Na_{0.05}Li_{0.86}MnO_{1.98}F_{0.02}$ samples subjected to 1 , 2, 5, 10, 20 and 30 cycles and 0.1mV/s over the potential range between 2.0 and 4.3 V (vs Li^+/Li). The striking feature is the difference between the first and subsequent cycles. In fact the difference is to be found in the original CV for $Na_{0.06}Li_{0.85}MnO_2$ shows two anodic peaks at 3.25 V and 4.18 V as well as the corresponding cathodic peaks at 2.83 V and 3.85 V. On repeated cycling, the peaks at 4.18 V and 3.85V split into two peaks, which becomes more obvious after 30 cycles. This peak splitting suggests a gradual transformation of layered $LiMnO_2$ into the spinel phase [34]. From Fig. 6(a), we can observe the anodic phase shows four oxidation peaks centered at 3.1 V, 4.0 V, 4.18 V, and 3.8 V after 2 cycles, but the cathodic phase shows only three reduction peaks with a major peak centered at 2.8 V and two minor peaks at 3.9 V and 4.1 V. The peak at 3.8 V does not have reduced peak, which corresponds to an irreversible phase change. Similar irreversible phase changes were observed by Paulsen et al. in O_2-type $Li_{2/3}[Li_{1/6}Mn_{5/6}]O_2$ and $Li_{2/3}[Co_{1/18}Mn_{17/18}]O_2$[39]. The reason for this irreversible peak/plateau is not presently known; however, because it is only observed in stacking faulted compounds, the irreversible peak could be correlated to crystallographic modification, oxygen removal from the lattice and/or removal of the stacking faults. For the $Na_{0.05}Li_{0.86}MnO_{1.98}F_{0.02}$ sample, the similar main cathodic and anodic peaks with $Na_{0.06}Li_{0.85}MnO_2$ sample in the first cycle are found in Fig.6 (b). From the CV curves of Fig.6 (b), Li^+ can mostly deintercalate from the structure of sample $Na_{0.05}Li_{0.86}MnO_{1.98}F_{0.02}$ in the first anode process, due to the broader oxidizing peak about 3.8 V. But the reducing peak about 2.9 V is weaker in the first cathode process. This result indicates there is obvious capacity loss between the initial charge and discharge capacities, and the efficiency of reversible intercalate/deintercalate of Li^+ is relatively lower, which is in accordance with Fig.4. As the cycle goes by, the intensity of oxidizing peak about 3 V gradually becomes stronger, and the intensities of reducing peak about 2.8 V and 4 V gradually become stronger. However, the anodic or cathodic current densities change slightly in the following cycles, evidencing the higher electrochemical stability of the $Na_{0.05}Li_{0.86}MnO_{1.98}F_{0.02}$ sample as compared to the $Na_{0.06}Li_{0.85}MnO_2$ sample.

The Fig. 5 also shows that the variation characteristics of capacity with cycle number for the $Na_{0.06}Li_{0.85}MnO_2$ and $Na_{0.05}Li_{0.86}MnO_{1.98}F_{0.02}$ materials. The first discharge of the $Na_{0.06}Li_{0.85}MnO_2$ sample is associated with a specific capacity of 133.2 mAh/g but this falls significantly to 117.7 mAh/g at the third cycle, then slowly increase the 190 mAh/g after 20 cycles and the subsequent decay slowly. For the $Na_{0.05}Li_{0.86}MnO_{1.98}F_{0.02}$ sample, the varying pattern is similar with the $Na_{0.06}Li_{0.85}MnO_2$ sample. The first specific capacity on discharge is 129.2 mAh/g but this falls significantly to 95 mAh/g at the 5th cycle, and subsequent slowly increase to 219 mAh/g after 40 cycles . However, the greatest difference can be found in the thereafter cycle process, the capacity on discharge is very similar at around 218 mAh/g. This is in accord with the CV in Fig. 6 and reinforces the view that the electrochemical evidence points to a change occurring during the first charge.

In order to further verify the results of electrochemical test and the influence of fluorine doping for the materials. The XRD was used to confirme by crystal structure measurements of the cycled cathode powder . Fig. 7 shows the XRD pattern of the $Na_{0.067}Li_{0.85}MnO_2$ and $Na_{0.05}Li_{0.86}MnO_{1.98}F_{0.02}$ subjected to 30 cycles. The diffraction peaks in the XRD pattern broadened after electrochemical cycling, which is attributed to the creation of local lattice strain and tiny crystallites during cycling[40].The results also show that the samples have been converted to the cubic spinel phase $LiMn_2O_4$ upon cycling, the results are consistent with the electrochemical experiments. However, The layered structure $LiMnO_2$ phase can obvious exist for the $Na_{0.05}Li_{0.86}MnO_{1.98}F_{0.02}$ materials in the electrochemical process . This fully shows that fluorine doping can effectively inhibit the structure of the shift.

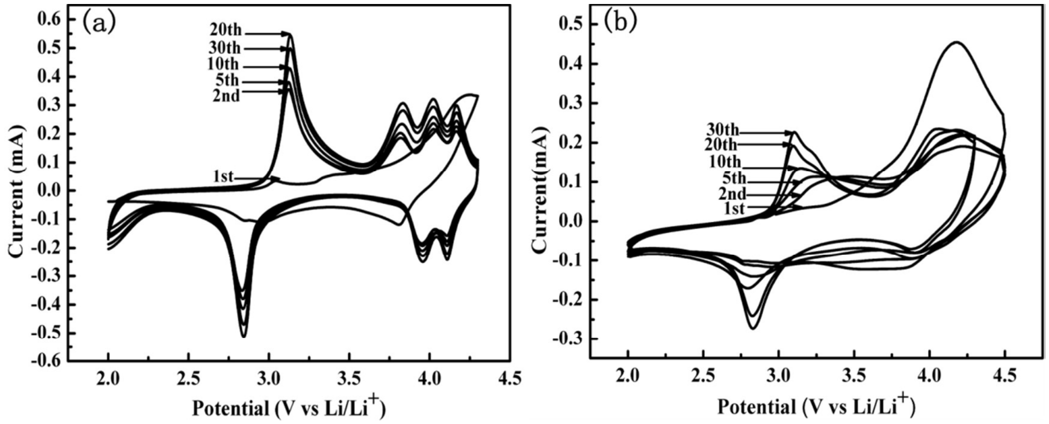

Fig. 6 Cyclic voltammograms of the (a) $Na_{0.067}Li_{0.85}MnO_2$ and (b) $Na_{0.05}Li_{0.86}MnO_{1.98}F_{0.02}$ subjected to 1, 2, 5, 10, 20 and 30 cycle.

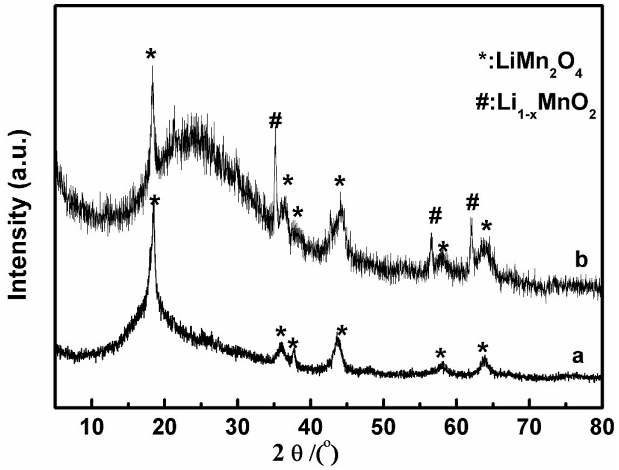

Fig. 7 XRD patterns of (a) $Na_{0.06}Li_{0.85}MnO_2$ and (b) $Na_{0.05}Li_{0.86}MnO_{1.98}F_{0.02}$ after 30 cycles

The Nyquist plots of the electrochemical impedance spectra (EIS) analyses are shown in Fig.8. All plots consist of both a semicircle in the high-frequency region and a slope in the low-frequency region. The electrode reaction process is primarily controlled by a mixed process of lithium ion diffusion (Warburg impedance, which is inversely proportional to the diffusion coefficient D_{Li+}) and the surface electrochemical reaction at a temporary steady state of EIS. Compared to the $Na_{0.07}Li_{0.85}MnO_2$ sample from Table 4, the Warburg impedance of fluorine-substituted materials is lower, which contributes to their improved high rate capability. On the contrary, the charge-transfer resistance increases after fluorine substitution due to the poor electrochemical activity of the anions, while the Warburg impedance obviously decreases as compared to that of the $Na_{0.07}Li_{0.85}MnO_2$ sample. Clearly, the Warburg impedance of the fluorine-substituted material $Na_{0.06}Li_{0.86}MnO_{1.98}F_{0.02}$ is much smaller than that of the $Na_{0.07}Li_{0.85}MnO_2$ sample, which is consistent with the improved high-rate capability demonstrated above.

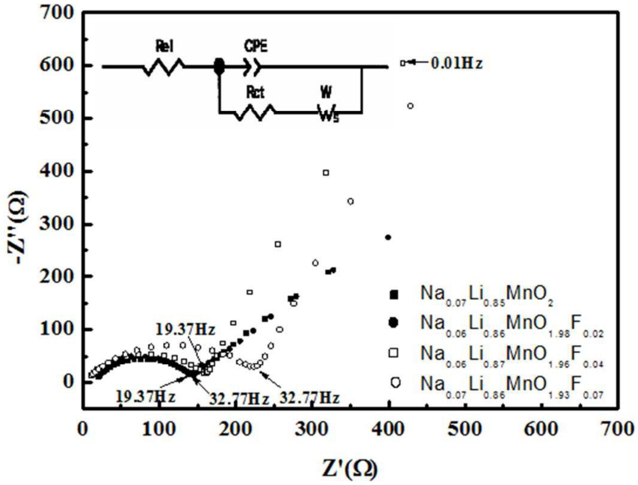

Fig. 8 Electrochemical impedance spectra (EIS) of the as-prepared samples at the discharged state (about 3.0 V (vs. Li^+/Li)) after the 30th cycle.

Table 4 Calculated electrochemical parameters from the AC impedance spectra of the ion-substituted Li_xMnO_2 samples using ZView 2.8 software.

Sample(ICP-AES)	R_{ct} (Ω)	CPE($\times10^{-5}$)	Ws(Ω)
$Na_{0.06}Li_{0.85}MnO_2$	122.31	1.04	270.71
$Na_{0.05}Li_{0.86}MnO_{1.98}F_{0.02}$	132.81	1.08	36.25
$Na_{0.06}Li_{0.88}MnO_{1.96}F_{0.04}$	152.91	1.05	112.32
$Na_{0.06}Li_{0.87}MnO_{1.93}F_{0.07}$	221.62	2.91	117.31

Note: R_{ct} represents the charge-transfer resistance, CPE represents the constant phase element, and Ws represents the Warburg impedance.

3.3 XPS spectra analysis of materials

The XPS spectra can provide chemical information such as the oxidation state as well as the semi-quantitative composition of the surface, thus enabling observation of the surface properties. Fig. 9 (a) shows the Mn 2p XPS spectra of the $Na_{0.05}Li_{0.86}MnO_{1.98}F_{0.02}$ sample. The binding energies of Mn $2P_{1/2}$ and Mn $2p_{3/2}$ were determined to be 653.86 eV and 641.80 eV, respectively. The peaks at the binding energy of about 641.60 eV are similar to those observed in Mn_2O_3 and MnOOH [41]. The binding energy peak situated at 653.86 is close to the binding energy of Mn $2P_{1/2}$ (653.90 eV) observed in the Mn_2O_3 sample. The binding energy of Na 1s was determined to be 1071.26, which is similar to that observed in NaF [42]. Moreover, the binding energy of F 1s is situated at 686.1 eV, which is similar to that observed at 686.1eV in MnF_2 [43]. To further determine the existence of fluorine within the crystal structure, XPS measurement was carried out on the four samples. Fig.9 (b) shows the XPS spectra of F 1s for the pristine and F-doped materials. All curve fittings were based on C 1s (C-C bonding energy) calibration to 284.5 eV. As shown in the figure, With the increase of the amount of F-doping, the area of the F 1s peak proportionately increases, reflecting an increase in the concentration of the fluorine ions in the doped material as the composition design. This observation is constant with the consecutive changes of lattice constants shown in Section 3.1, which further proves that the fluorine ions have been successfully doped into the lattice structure.

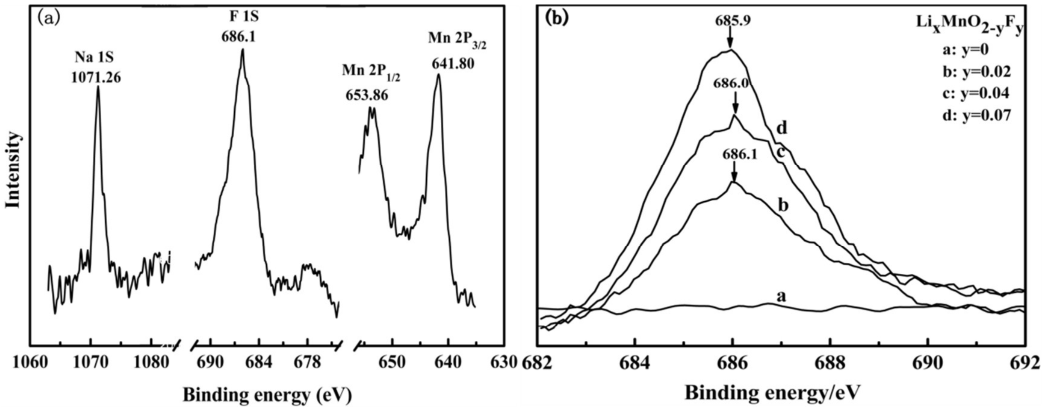

Fig. 9 The XPS spectra of the $Na_{0.06}Li_{0.86}MnO_{1.98}F_{0.02}$ sample and F 1s for $Li_xMnO_{2-y}F_y$

4. Conclusion

The fluorine doped monoclinic $LiMnO_2$ could be successfully synthesized via a high-temperature solid-state reaction and subsequent ion exchange by hydrothermal method. The partial fluorine substitution with high electronegativity anions strengthens the Mn-O bands in the layered monoclinic structure, which stabilizes the structure. Though the F-doped samples had lower initial capacities, they showed better cycle performance compared with F-free samples. The $Na_{0.05}Li_{0.86}MnO_{1.98}F_{0.02}$ electrode delivers an initial discharge capacity of 129.2 mAh/g between 2 and 4.3 V at a current density of 50 mA/g at room temperature, which gradually increased to a maximum discharge capacity of 219 mAh/g after 40 cycles. The research indicated that the different performances can be attributed to the different morphologies of the respective materials as well as the effect of sodium ion concentration within the structure. Therefore, controlling the morphology of the material and the amount of sodium ions in its structure may be advantageous for developing high quality cathode materials which can be diversified for specific applications in Li-ion batteries.

Acknowledgements

This work was supported by The National Natural Science Foundation of China (21061015) and The nature science foundation from Xinjiang autonomous region (2015211A037).

References

[1] J. Reed, G .Ceder, *Chem. Rev.*, 104 (2004)4513-4534.

[2] P. Suresh ,A. K. Shukla, N. Munichandraiah, *Electrochem. Solid State Lett.*,8 (2005) A263-A266.

[3] B. Ammundsen, J. Desilvestro., T. Groutso, D. Hassell, J. B. Metson, E. Regan, R. Steiner, P.J .Pickering, *J. Electrochem. Soc*.,147 (2000) 4078-4082.

[4] J. E. Greedan, N. P. Raju, I. J. Davidson, *J. Solid State Chem.* 128 (1997) 209-214.

[5] Y. J. Wei, H. Ehrenberg, N. N. Bramnik, K. Nikolowski, C. Baehtz, H. Fuess, *Solid State Ionics*,178 (2007) 253-257.

[6] T. J. Kim, D. Son, J. Cho, B. Park, *J. Power Sources,* 154 (2006) 268-272.

[7] A. R. Armstrong, P. G. Bruce, *Nature*, 381 (1996) 499-500.

[8] F. Capitaine, P. Gravereau, C. Delmas, *Solid State Ionics*, 89 (1996) 197-202.

[9] Z. F. Huang, X. Meng, C. Z. Wang, Y. Sun, G. Chen, *J. Power Sources* 158 (2006) 1394-1400.

[10] R. Prasad, R. Benedek, M. M. Thackeray, *Phys. Rev. B* 71 (2005) 134111.

[11] G. Ceder, S. K. Mishra, *Electrochem. Solid-State Lett.* 2 (1999) 550-552.

[12] C. W. Park, I. R. Mangani, H. W. Ryu, C. J. Park, J. S. Lee, S. J. Song, J. H. Moon, J. Kim, *J. Phys. Chem. Solids,* 68 (2007) 1126-1130.

[13] A. D. Robertson, A. R. Armstrong, P. G. Bruce, *Chem. Mater*,13 (2001) 2380.

[14] L. H. Yu, H. X. Yang, X. P. Ai, Y. L. Cao, *J. Phys. Chem. B*, 109 (2005) 1148-1154.

[15]S.B. Patoux, M. Dolle, M. M. Doeff, *Chem. Mater*. 17 (2005) 1044-1054.

[16] J. H. Kim, C. W. Park, Y. K. Sun, *Solid State Ion*, 164 (2003) 43-49 .

[17] B. J. Hwang, Y. W. Tsai, C. H. Chen, R. Santhanam, *J. Mater. Chem.*, 13 (2003) 1962-1968.

[18]W.K. Pang, J.Y. Lee, Y.S. Wei, S.H. Wu , *Mater. Chem. Phys*.,139(2013)241-246.

[19] G. H. Kim, S. T. Myung, H. S. Kim, C. S. Yoon, Y. K. Sun, *J. Electrochem. Soc.,* 152 (2005) A1707-A1713.

[20]J.M. Zheng, X.B. Wu, Y. Yang, *Electrochim Acta* 105 (2013) 200– 208.

[21]S.Jouanneau., J.R.Dahn, *J. Electrochem. Soc.,* 151(2004)A1749-A1754.

[22]Q. G. Zhang, T. Y. Peng, D Zhan, X H Hu,*J. Power Sources*,250(2014) 40-49.

[23]J. L. Xie, X. Huang, Z. B. Zhu, J. H Dai , *Ceram. Int.*, 37(2011)419-421.

[24] W.S. Fyfe,.Anal. Chem. , 1951 , 23(1):174 -175 .

[25] R. Chitrakar, H. Kanoh, Y. S. Kim, Y. Miyai, K.Ooi, *J. Solid State Chem*. ,160 (2001) 69-76.

[26] S.H. Kang, I. Belharouak, Y.K. Sun, K. Amine, *J. Power Sources* 146 (2005) 650–653.

[27] P. Barboux , J. M. Tarascon, F. K. Shokoohi, *J. Solid State Chem.* 94 (1991) 185-196.

[28] E. Wolska, P. Piszora, W. Nowicki, J. Darul, *Int J. Inorg Mater,* 6(2001)503-507.

[29] L. K. Kang, M. M. Zhang, Z. H. Liu, K. Ooi,*Spectrochim Acta A* 67 (2007) 864-869.

[30] H. D. B. Jenkins, H. K. Roobottom, J. Passmore, L. Glasser, *Inorg. Chem*. 38 (1999) 3609-3620.

[31] X.Q. Wang, H. Nakamura, M. Yoshio, J. Power Sources 110 (2002) 19–26.

[32]Y.-S. He, L. Pei, X.-Z. Liao, Z.-F. Ma, S, J. Fluorine Chem., 128 (2007) 139-143.

[33]S.W. Oh, S.H. Park, J.H. Kim, Y. C. Bae, Y. K. Sun, J. Power Sources, 157 (2006) 464-470.

[34] G.H. Kim, M.H. Kim, S.T. Myung, Y.K. Sun, *J. Power Sources* ,146 (2005) 602-605.

[35] Y.S. He, L. Pei, X. Z. Liao, Z.F. Ma, *J. Fluorine Chem.*, 128 (2007) 139-143.

[36]Y-II Jang, B.Y.Huang, H.F.Wang, R.S.Donald, Y.M.Chiang, J. *Electrochem. Soc.,*146 (9) (1999) 3217-3223.

[37] P.Yue, Z.X. Wang, X.H. Li, X.H. Xiong, J.X. Wang, X.W.Wu, H.J Guo, *Electrochim Acta* ,95 (2013) 112- 118.

[38] S. Bach, J.P. Pereira-Ramos P. Willmann, *Electrochim Acta* 52 (2006) 504-510.

[39] J. M. Paulsen, C. L. Thomas, J. R. Dahn, *J. Electrochem. Soc.*146 (1999) 3560-3565.

[40] S. W.Mai, M. Q.Xu, X. L. Liao, L. D. Xing, W. S. Li, J. Power Sources, 273(2015)816-822.

[41] B. J. Tan, K. J. Klabunde, P. M. A. Sherwood, *J. Am. Chem. Soc.*113 (1991) 855-861.

[42]V. I. Nefedov, Y. V. Salyn, G. Leonhsardt, R. Scheibe, *J. Electron Spectrosc. Relat. Phonom.* ,10 (1997) 121-124.

[43] R. G. Hayes, N. Edelstein, D. A. Shirley Ed. *Electro.n Spectroscopy*, North-Holland Publishing Company, Amsterdam,771-781(1972).

Table 1 Chemical composition of the *m*-$LiMnO_2$ and F-substituted *m*-$LiMnO_2$.

Sample	Design formula	Precursor powders	Valence of manganese	Chemical composition
a	$NaMnO_2$	$Na_{0.96}MnO_2$	3.04	$Na_{0.96}MnO_2$
b	$LiMnO_2$	$Na_{0.91}MnO_2$	3.09	$Na_{0.06}Li_{0.85}MnO_2$
c	$LiMnO_{1.99}F_{0.01}$	$Na_{0.90}MnO_{1.98}F_{0.02}$	3.08	$Na_{0.05}Li_{0.86}MnO_{1.98}F_{0.02}$
d	$LiMnO_{1.97}F_{0.03}$	$Na_{0.91}MnO_{1.96}F_{0.04}$	3.05	$Na_{0.06}Li_{0.88}MnO_{1.96}F_{0.04}$
e	$LiMnO_{1.95}F_{0.05}$	$Na_{0.92}MnO_{1.93}F_{0.07}$	3.01	$Na_{0.06}Li_{0.87}MnO_{1.93}F_{0.07}$

Table 2 Comparison between the observed and JCPDS-871255 values

	$d_{hkl}(LiMnO_2)$/nm		2θ/(°)	
h k l	Observed	JCPDS	Observed	JCPDS
0 0 1	0.4849	0.4842	18.28	18.31
-2 0 1	0.2712	0.2711	33.02	33.01
1 1 0	0.2440	0.2435	36.80	36.89
-1 1 1	0.2397	0.2395	37.48	37.50
-2 0 2	0.2298	0.2295	39.12	39.21
1 1 1	0.2012	0.2006	45.02	45.15
-1 1 2	0.1942	0.1942	46.46	46.74
2 0 1	0.1878	0.1875	48.45	48.49
0 0 3	0.1626	0.1614	56.52	57.01
1 1 2	0.1560	0.1555	59.16	59.37
-1 1 3	0.1511	0.1505	61.26	61.56
-3 1 2	0.1493	0.1487	62.12	62.36
0 2 0	0.1407	0.1404	66.34	66.53
0 2 1	0.1350	0.1348	69.54	69.66

Table 3 Lattice parameters of the samples after Rietveld refinement.

Sample	a(nm)	b(nm)	c(nm)	cell volume(nm^3)
$Na_{0.96}MnO_2$	0.582	0.287	0.576	0.0962
$Na_{0.06}Li_{0.85}MnO_2$	0.544	0.281	0.539	0.0824
$Na_{0.05}Li_{0.86}MnO_{1.98}F_{0.02}$	0.543	0.282	0.541	0.0828
$Na_{0.06}Li_{0.88}MnO_{1.96}F_{0.04}$	0.543	0.282	0.543	0.0831
$Na_{0.06}Li_{0.87}MnO_{1.93}F_{0.07}$	0.544	0.283	0.549	0.0839

Table 4 Calculated electrochemical parameters from the AC impedance spectra of the ion-substituted Li_xMnO_2 samples using ZView 2.8 software.

Sample(ICP-AES)	R_{ct} ( )	CPE($\times 10^{-5}$)	Ws( )
$Na_{0.06}Li_{0.85}MnO_2$	122.31	1.04	270.71
$Na_{0.05}Li_{0.86}MnO_{1.98}F_{0.02}$	132.81	1.08	36.25
$Na_{0.06}Li_{0.88}MnO_{1.96}F_{0.04}$	152.91	1.05	112.32
$Na_{0.06}Li_{0.87}MnO_{1.93}F_{0.07}$	221.62	2.91	117.31

Note: R_{ct} represents the charge-transfer resistance, CPE represents the constant phase element, and Ws represents the Warburg impedance.

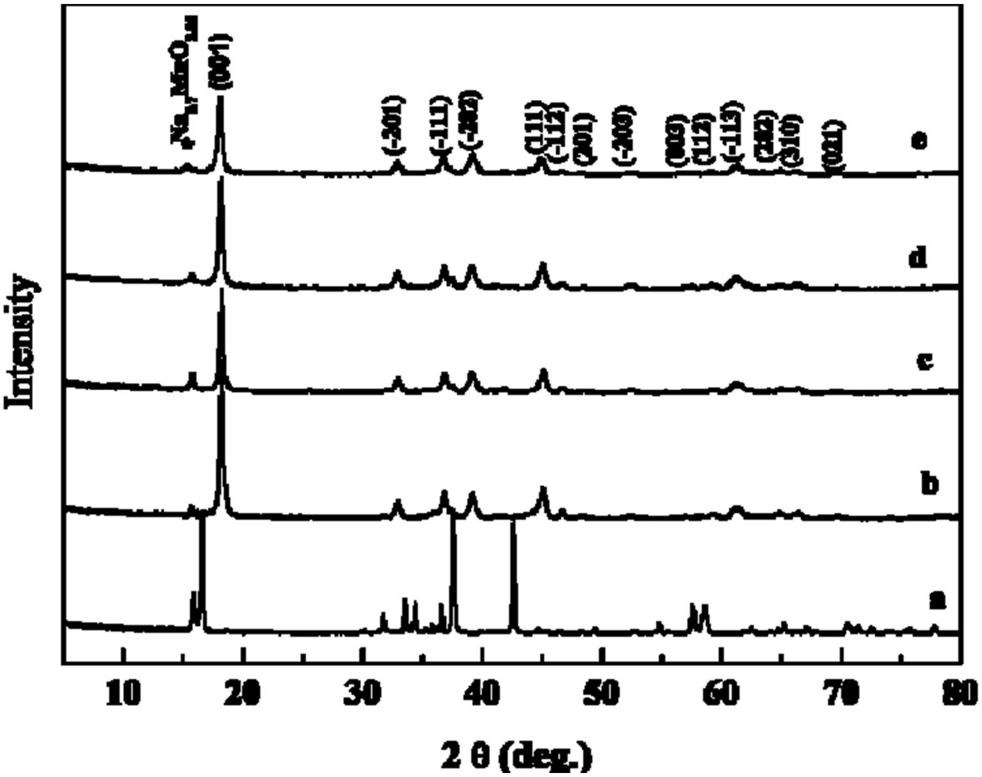

130x100mm (150 x 150 DPI)

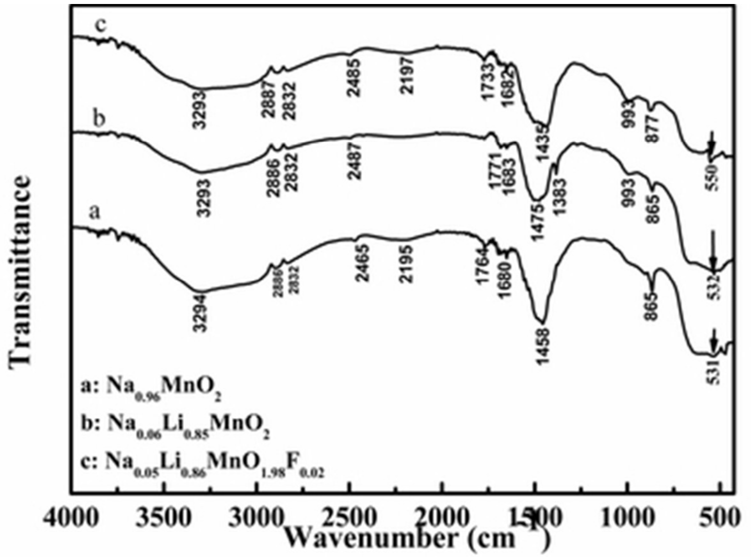

31x23mm (300 x 300 DPI)

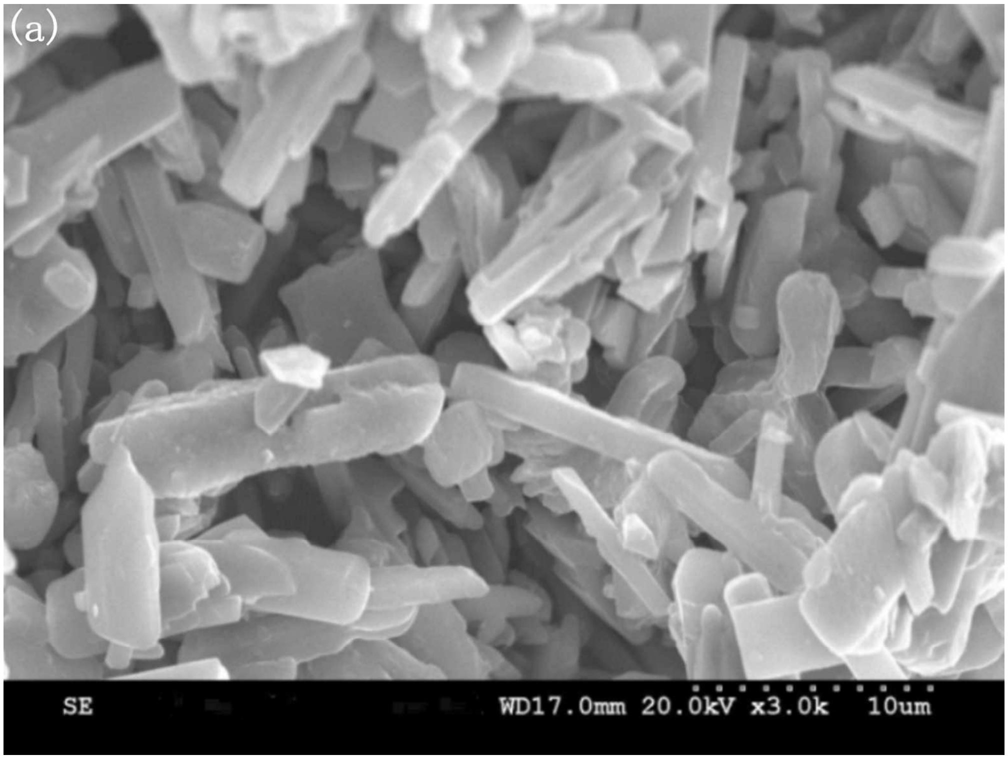

338x254mm (150 x 150 DPI)

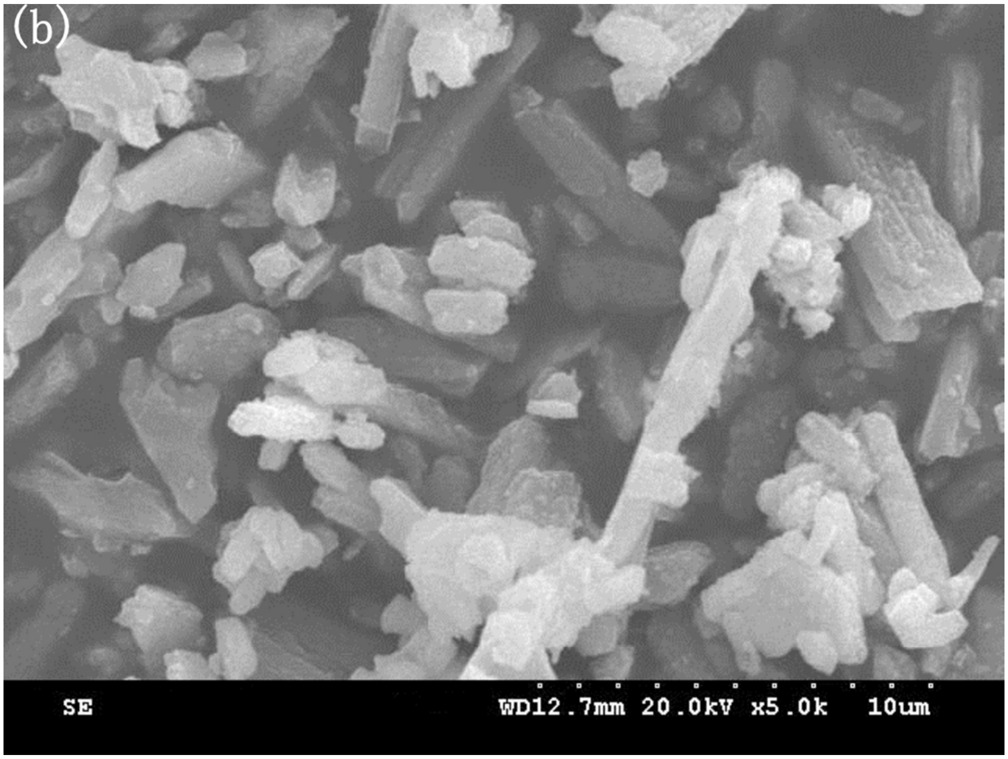

169x127mm (150 x 150 DPI)

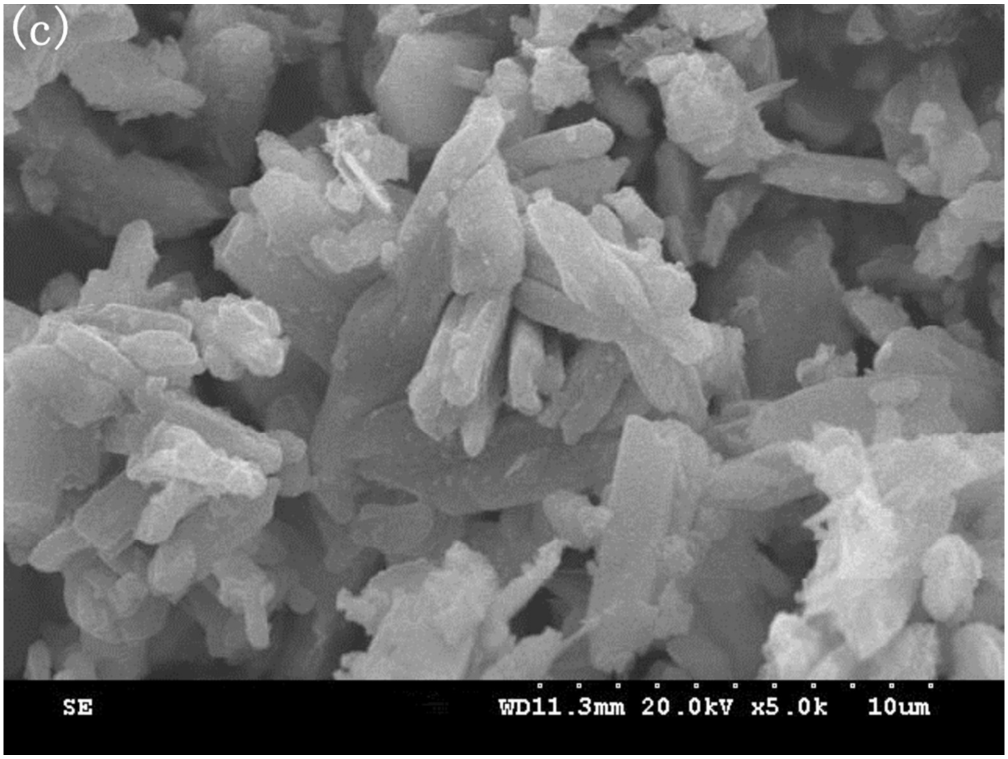

169x127mm (150 x 150 DPI)

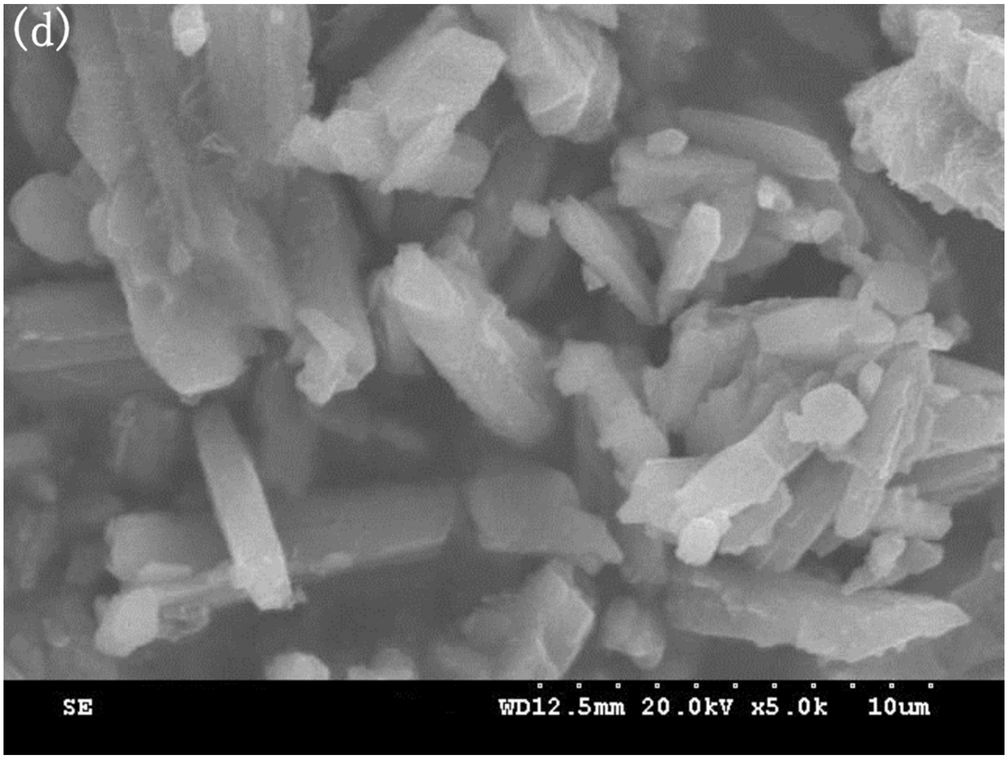

169x127mm (150 x 150 DPI)

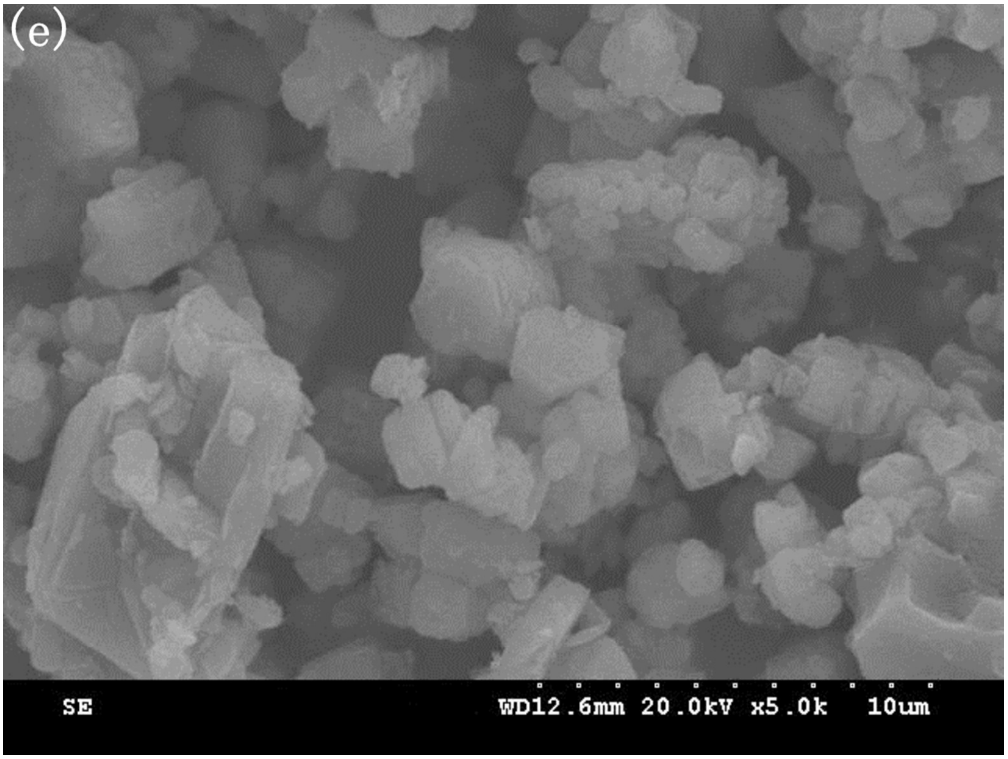

169x127mm (150 x 150 DPI)

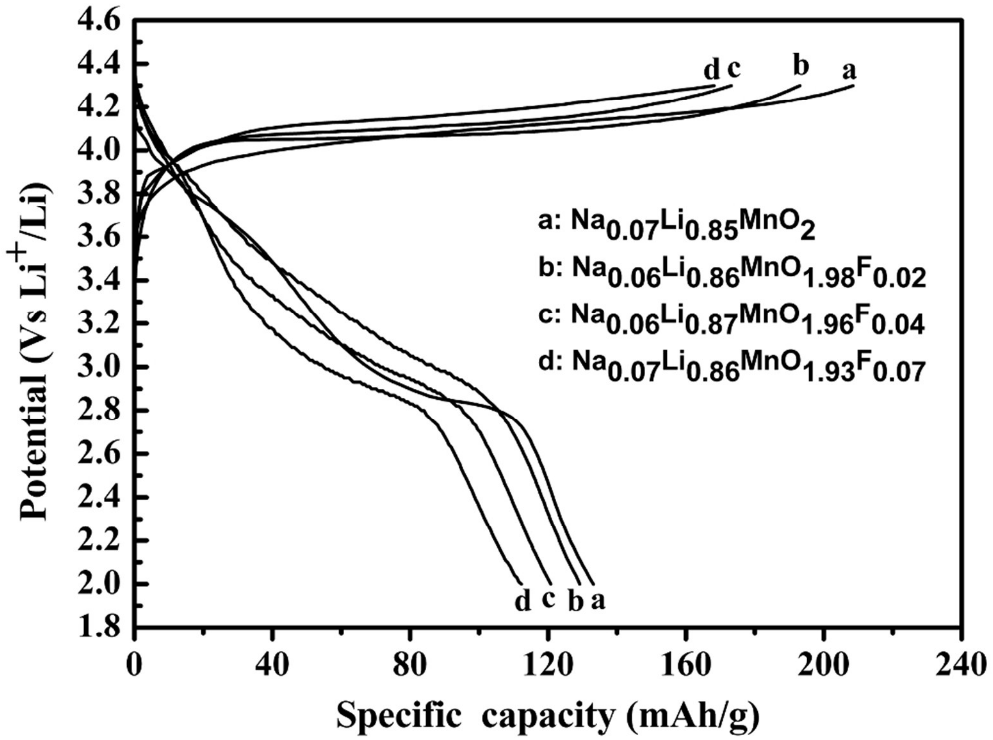

173x129mm (150 x 150 DPI)

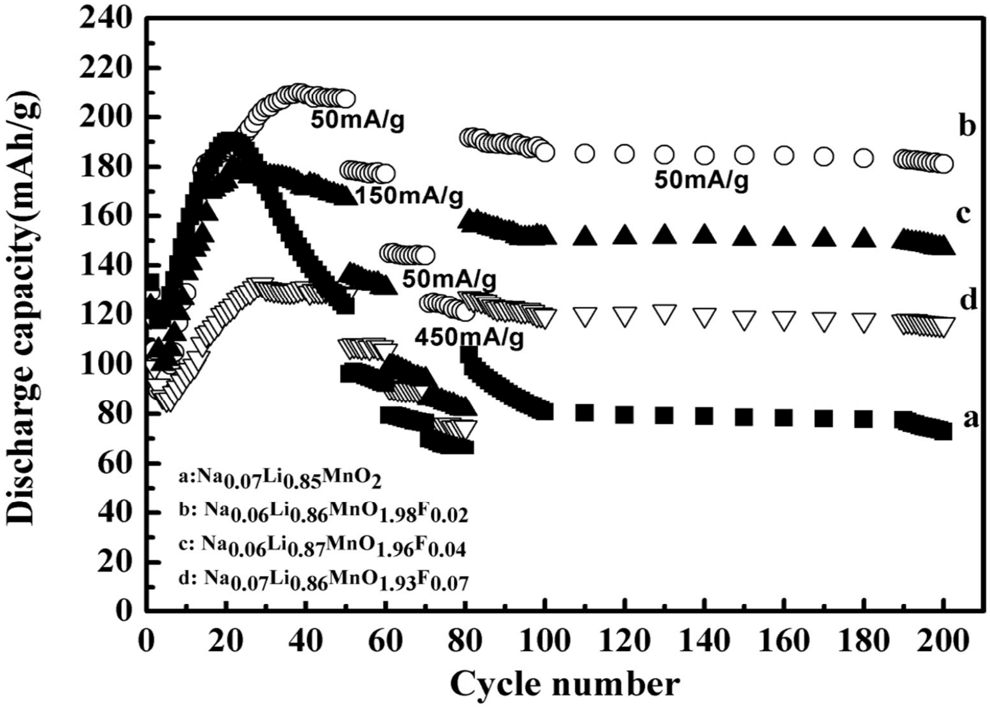

109x78mm (300 x 300 DPI)

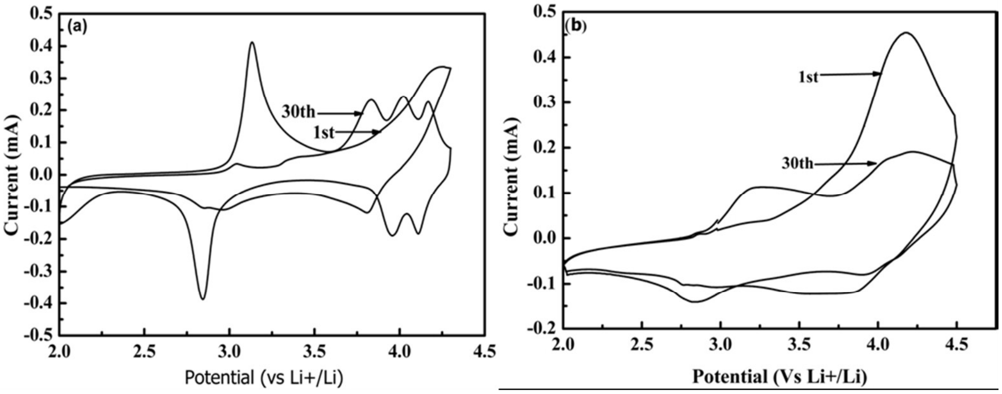

173x67mm (150 x 150 DPI)

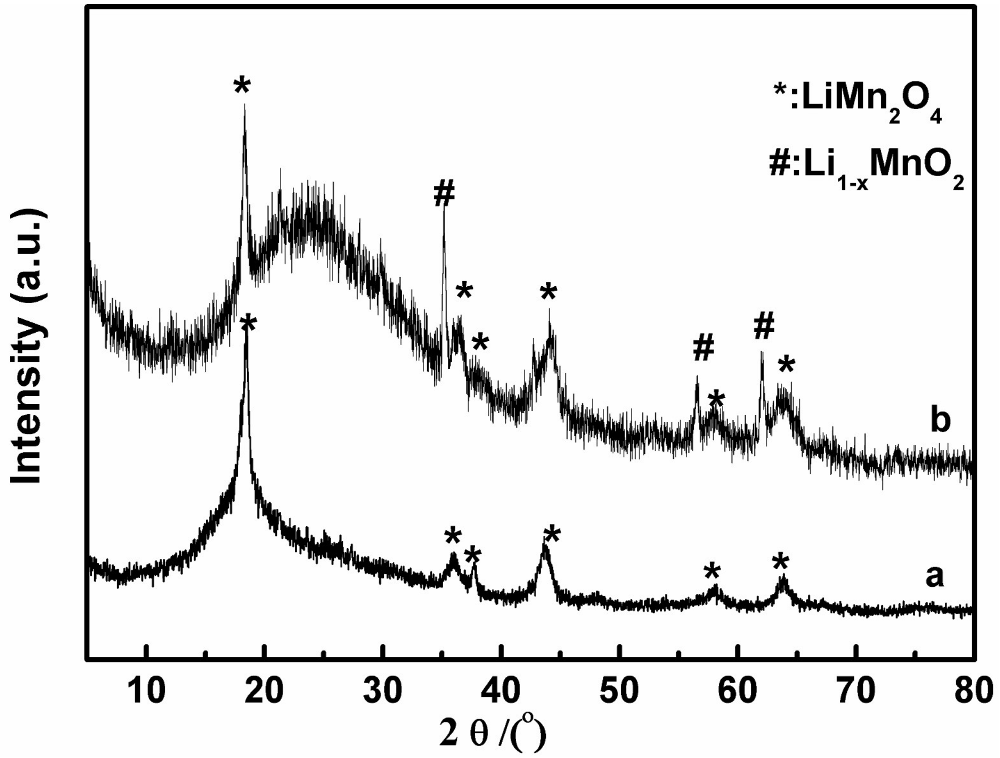

297x223mm (300 x 300 DPI)

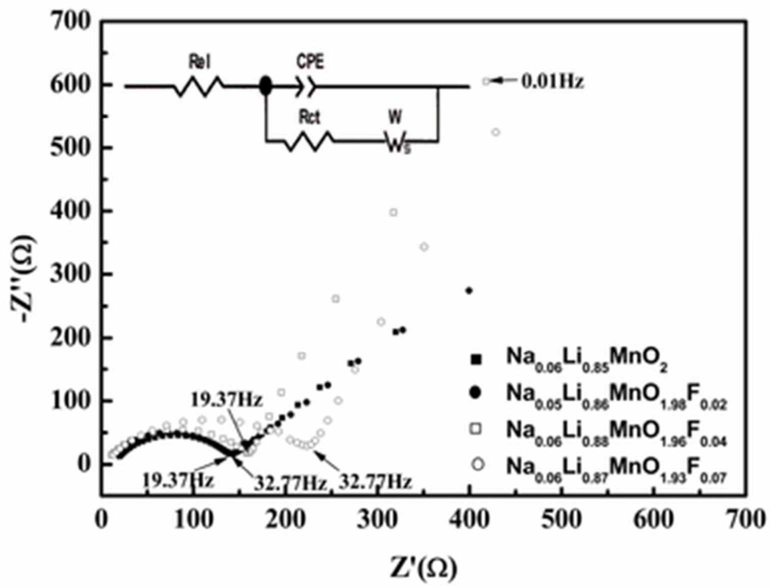

16x12mm (600 x 600 DPI)

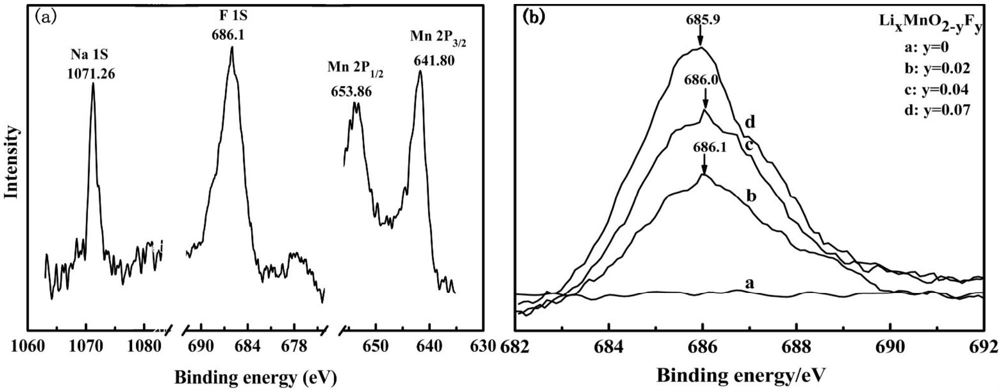

594x228mm (150 x 150 DPI)